Computers and Mathematics with Applications 70 (2015) 1220–1233

Contents lists available at ScienceDirect

Computers and Mathematics with Applications

journal homepage: www.elsevier.com/locate/camwa

Computation of fixed boundary tokamak equilibria using a method based on approximate particular solutions

D. Nath *, M.S. Kalra, P. Munshi

Nuclear Engineering and Technology Program, Indian Institute of Technology Kanpur, Kanpur - 208 016, India

ARTICLE INFO

Article history:
Received 5 December 2014
Received in revised form 9 July 2015
Accepted 14 July 2015
Available online 3 August 2015

Keywords:
Grad-Shafranov equation
Tokamak plasma equilibrium
Meshless method
Method of approximate particular solutions

ABSTRACT

In this work a meshless method based on the approximate particular solutions is applied to the computation of fixed boundary tokamak equilibria using Grad–Shafranov (GS) equation. The GS equation is solved for different choices of the right hand side of the equation: (i) when it is not a function of magnetic flux (i.e., Solov'ev solutions), (ii) when it is a linear function of magnetic flux, and (iii) when it is a nonlinear function of magnetic flux. For all these cases the first order derivative term in the GS equation is transferred to the right hand side such that the left hand side consists only the Laplace operator. This enables us to use the Radial Basis Functions (RBFs) in the calculation of approximate particular solutions. A linear combination of these particular solutions is taken as the solution of the GS equation and the resulting system of algebraic equations is solved iteratively because of the presence of the magnetic flux on the right hand side in all three choices. Furthermore, we use least squares approach in solving the overdetermined system of algebraic equations which alleviates the problem of ill-conditioning to a certain extent. The numerical results obtained using this method are in good agreement with the analytical solutions (where available). We find that the method is convergent, accurate and easily applicable to the irregular geometries due to its meshless character.

1. Introduction

The Magnetohydrodynamic (MHD) equilibria in the tokamak are described by the Grad–Shafranov (GS) equation [1]. This is in general a nonlinear elliptic partial differential equation derived from the ideal MHD equations. There are numerous extensive works in the literature for solving GS equation for the fixed and free boundary problems in the tokamak using the finite element, finite difference, spectral, boundary element and other mesh based methods [2–9]. However the work based on meshless methods applied to the GS equation is very limited. Some of these works are given in [10–12]. The meshless methods have the advantages that (i) they are comparatively easy to program, (ii) they do not require a mesh, and (iii) they can be applied to any geometry without much difficulty.

The aim of the present work is to formulate and apply a meshless method based on the approximate particular solutions for the computation of the fixed boundary tokamak equilibria. The governing equation consists of an axisymmetric operator on the left hand side of an elliptic partial differential equation. Although the GS operator is linear, to find its particular solution is very hard except for some cases when the right hand side is a combination of monomials or some other simple function [13]. Furthermore, if the approximate particular solutions are obtained by approximating the right hand side by radial basis functions (RBFs), then these particular solutions no longer remain purely radial functions, i.e., they contain both

* Corresponding author. Fax: +91 512 2597408.
E-mail addresses: dnath@iitk.ac.in (D. Nath), msk@iitk.ac.in (M.S. Kalra), pmunshi@iitk.ac.in (P. Munshi).

http://dx.doi.org/10.1016/j.camwa.2015.07.013
0898-1221/

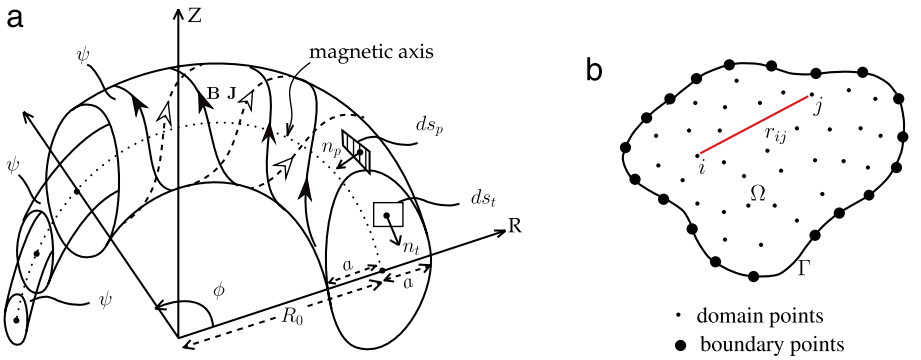

Fig. 1. (a) A torus showing flux surfaces (ψ = constant) on which **B** and **J** lie, (b) a schematic representation of domain and boundary on a poloidal cross-section.

coordinates (x and y) instead of being a function of radial distance only. In this work we rearrange the GS equation such that its left hand side consists of only the Laplace operator and the remaining term is transferred to the right hand side. This allows the particular solutions to be purely RBFs. The requirement of particular solutions to be RBFs is because the RBF interpolants possess certain important properties namely radial symmetry and invariance under translations, rotations, and reflections [14].

The linear combination of such particular solutions (associated with each node) is used to express the solution of the GS equation. It is noted that the fundamental solution which is needed for the calculation of homogeneous solution, as in the method of fundamental solutions (MFS) [15,12,16], is no longer needed in the present method. The present method was originally developed in [17] and named as MAPS (Method of Approximate Particular Solutions). We have applied it to the present problem in a least squares sense. The least squares method helps to alleviate the ill-conditioning (which is inherent in meshless methods) to a certain extent. The multiquadratic (MQ)-RBF has been used in the following calculations due to its better performance among the other globally supported RBFs [18,19].

In Section 2, the GS equation is presented in a nondimensional form. In Section 3, the least squares method based on the approximate particular solutions is presented to solve the GS equation numerically. In Section 4, the results are shown corresponding to the three choices of right hand side of the GS equation: (a) when it is not a function of magnetic flux (Ψ) (Solov'ev case), (b) when it is a linear function of Ψ, and (c) when it is a nonlinear function of Ψ. The conclusions are given in Section 5.

2. The Grad–Shafranov equation

The Grad–Shafranov equation is derived from the steady state ideal MHD equations in cylindrical coordinates (R, Z, ϕ) with the assumption of toroidal symmetry ($\partial/\partial\phi = 0$) and static plasma ($\boldsymbol{v} = 0$) and can be written as follows [2,9]:

$$-\left\{R\frac{\partial}{\partial R}\left(\frac{1}{R}\frac{\partial\Psi}{\partial R}\right)+\frac{\partial^2\Psi}{\partial Z^2}\right\} = \mu_0 R^2\frac{dp(\Psi)}{d\Psi}+I(\psi)\frac{dI(\Psi)}{d\Psi} \equiv \mu_0 R J_\phi \tag{1}$$

where J_ϕ = toroidal component of the current density and μ_0 = magnetic permeability of free space. The magnetic flux Ψ in Eq. (1) is the poloidal flux Ψ_p normalized by 2π, i.e.,

$$\Psi = \frac{1}{2\pi}\int_{s_p}\mathbf{B}\cdot\mathbf{n}ds_p$$

where **B** is the magnetic field, **n** is the unit normal to a surface element ds_p as shown in Fig. 1(a). In Eq. (1) $p(\Psi)$ is the pressure as a function of Ψ, $I(\Psi)$ is the poloidal current function defined by $I(\Psi) = \int_{s_p}\mathbf{J}\cdot\mathbf{n}ds_p$ where **J** is the current density. The quantity $\Psi \equiv \Psi(R, Z)$ gives the equilibrium profile of the plasma in the geometry under consideration.

Nondimensionalisation

The GS equation (Eq. (1)) can be nondimensionalized using: $x = R/R_0$, $y = Z/R_0$, $\psi = \Psi/\Psi_0$, $B_x = B_R/\left(\Psi_0/R_0^2\right)$, $B_y = B_Z/\left(\Psi_0/R_0^2\right)$ and $j_\phi = \left(\mu_0 R_0^3/\Psi_0\right)J_\phi$, where R_0 is the major radius and Ψ_0 is an arbitrary value of the magnetic flux. In other words, using $R \to xR_0$, $Z \to yR_0$, $\Psi \to \Psi_0\psi$, $B_R \to \left(\Psi_0/R_0^2\right)B_x$, $B_Z \to \left(\Psi_0/R_0^2\right)B_y$ and $J_\phi \to \left(\Psi_0/\mu_0 R_0^3\right)j_\phi$, the GS equation can be written in the following nondimensional form:

$$-\triangle^*\psi \equiv -\left\{x\frac{\partial}{\partial x}\left(\frac{1}{x}\frac{\partial\psi}{\partial x}\right)+\frac{\partial^2\psi}{\partial y^2}\right\} = xj_\phi \equiv \mathcal{F}(\psi, x, y), \tag{2}$$

where $\triangle^*$ is the Grad–Shafranov operator. The above equation can be rearranged as,

$$\frac{\partial^2\psi}{\partial x^2} + \frac{\partial^2\psi}{\partial y^2} = -\mathcal{F}(\psi, x, y) + \frac{1}{x}\frac{\partial\psi}{\partial x}$$

or,

$$\nabla^2\psi = g, \tag{3}$$

where ∇^2 is the two-dimensional Laplacian operator in Cartesian coordinates, and

$$g = -\mathcal{F}(\psi, x, y) + \frac{1}{x}\frac{\partial\psi}{\partial x}. \tag{4}$$

3. Numerical formulation of Grad–Shafranov equation

In general the solution of a partial differential equation (PDE) is represented as a sum of an exact particular solution and an arbitrary number of homogeneous solutions. However in the MAPS the homogeneous solutions are omitted completely and the solution is written as a linear combination of approximate particular solutions using RBFs [17,19]. Consider a domain Ω surrounded by the boundary Γ (Fig. 1(b)) having n_d number of domain points, n_b number of boundary points, and n_t $(= n_d + n_b)$ number of total points. The distance between the node i and j is given by the radial distance r_{ij}. The numerical solution of Eq. (3) can be expressed as a linear combination of approximate particular solutions, $\hat{\psi}_{ij}$, as below:

$$\psi_j = \sum_{i=1}^{n_d} a_i\hat{\psi}_{ij}, \quad j = 1, 2, \ldots, n_d. \tag{5}$$

where a_i's are the coefficients to be determined and $\hat{\psi}_{ij}$ are given by

$$\left(\nabla^2\hat{\psi}\right)_{ij} = f_{ij} \tag{6}$$

when f_{ij} are the chosen RBFs in domain Ω, such that,

$$g_j \simeq \sum_{i=1}^{n_d} a_i f_{ij} \quad j = 1, 2, \ldots, n_d. \tag{7}$$

In the present work, we choose the multiquadratic (MQ)-RBF,

$$f_{ij} = \sqrt{r_{ij}^2 + \sigma^2} \tag{8}$$

where σ is the *shape parameter*, $r_{ij} = \sqrt{(x_i - x_j)^2 + (y_i - y_j)^2}$ is the radial distance (Fig. 1(b)), (x_j, y_j) are the RBF centers and (x_i, y_i) are arbitrary points in the domain under consideration. For the RBFs, f_{ij}, the expressions for particular solutions $\hat{\psi}_{ij}$ can be obtained using the two-dimensional Laplacian in radial coordinates, i.e., $\nabla^2 = \frac{1}{r}\frac{d}{dr}\left(r\frac{d}{dr}\right)$ [20]. These together with their derivatives with respect to x and y are given in the Appendix A. Substituting Eq. (5) in Eq. (3), we get:

$$\sum_{i=1}^{n_d} a_i\left(\nabla^2\hat{\psi}\right)_{ij} = g_j \quad j = 1, 2, \ldots, n_d.$$

Making use of Eq. (6) in the above equation, we can get following equations for the domain points:

$$\sum_{i=1}^{n_d} a_i f_{ij} = g_j \quad j = 1, 2, \ldots, n_d. \tag{9}$$

The Dirichlet boundary condition on the boundary Γ, $\psi = \psi_\Gamma = \bar{\psi}$ (say), can be incorporated by applying Eq. (5) to the boundary points:

$$\sum_{i=1}^{n_d} a_i\hat{\psi}_{ij} = \bar{\psi}_j, \quad j = 1, 2, \ldots, n_b. \tag{10}$$

(In this method the Neumann boundary condition is equally easy to apply as the derivatives of $\hat{\psi}_{ij}$ are known). Finally Eqs. (9) and (10) are combined to yield the following system of algebraic equations:

$$\begin{bmatrix} [\mathrm{F}]_{n_d\times n_d} \\ \left[\hat{\Psi}\right]_{n_b\times n_d} \end{bmatrix}_{n_t\times n_d} \{a\}_{n_d\times 1} = \begin{Bmatrix} \{g\}_{n_d\times 1} \\ \left\{\bar{\psi}\right\}_{n_b\times 1} \end{Bmatrix}_{n_t\times 1},$$

which can be expressed in the following form

$$[\mathrm{A}]\{a\} = \{b\} \tag{11}$$

where $\{b\} = \left\{\{g\}, \left\{\bar{\psi}\right\}\right\}^{\mathrm{T}}$, [F] is the matrix of RBFs f_{ij}, and $\left[\hat{\Psi}\right]$ is matrix of particular solutions $\hat{\psi}_{ij}$. The derivatives of ψ can be calculated using the derivatives of approximate particular solution as:

$$\left(\frac{\partial \psi}{\partial x}\right)_j = \sum_{i=1}^{n_d} a_i \left(\frac{\partial \hat{\psi}}{\partial x}\right)_{ij}, \quad j = 1, 2, \ldots, n_d, \tag{12}$$

$$\left(\frac{\partial \psi}{\partial y}\right)_j = \sum_{i=1}^{n_d} a_i \left(\frac{\partial \hat{\psi}}{\partial y}\right)_{ij}, \quad j = 1, 2, \ldots, n_d. \tag{13}$$

For MQ-RBFs used in this work, these derivatives are given in Appendix A. The overdetermined system of equations (Eq. (11)) is solved by the method of least squares which minimizes the norm $\|Aa - b\|_{L^2}$ using QR factorization of matrix [A]. (In MATLAB the operator "\" is used for this purpose [21].) The solution ψ can now be written as:

$$\psi_j \simeq \sum_{i=1}^{n_d} a_i \hat{\psi}_{ij}, \quad j = 1, 2, \ldots, n_t. \tag{14}$$

The following choices of the right hand side of the GS equation (Eq. (2)) are considered in the present work: (i) right hand side is a function of x and y and not a function of ψ which corresponds to the Solov'ev solutions [22], (ii) right hand side is a linear function of ψ but not proportional to ψ so that $\psi = 0$ is *not* a solution, and (iii) right hand side is a nonlinear function of ψ such that $\psi = 0$ is a (trivial) solution. It may be noted that due to the rearrangement of GS operator, the right hand side always contains ψ which makes the solution procedure iterative in all the three cases. In choices (i) and (ii) of the right hand side, the Picard iterations shown below, are sufficient and the solution converges:

$$\nabla^2 \psi^{(n+1)} = -\mathcal{F}\left(\psi^{(n)}, x, y\right) + \frac{1}{x}\frac{\partial \psi^{(n)}}{\partial x} \equiv g^{(n)}. \tag{15}$$

The superscript$^{(n)}$ represents the nth iteration. The solution of above equation can be obtained using Eq. (11) which takes the following form:

$$[A]\{a\}^{(n+1)} = \{b\}^{(n)} \tag{16}$$

and then $\psi_j^{(n+1)}$ can be obtained using Eq. (14) as,

$$\psi_j^{(n+1)} = \sum_{i=1}^{n_d} a_i^{(n+1)} \hat{\psi}_{ij}, \quad j = 1, 2, \ldots, n_t. \tag{17}$$

The iterations are stopped when the L^∞-error, E, defined by,

$$\mathrm{E} = \frac{\left\|\psi^{(n+1)} - \psi_{exact}\right\|_{L^\infty}}{\left\|\psi_{exact}\right\|_{L^\infty}} \tag{18}$$

achieves a certain minimum value.

If the right hand side of the GS equation is such that $\psi = 0$ is a (trivial) solution, the inverse iteration algorithm based on simultaneous evolution of eigen pair $(\lambda^{(n)}, \psi^{(n)})$ as given in [7] is used to find the smallest eigen value and the corresponding eigen function. (Alternative algorithms based on a power iterative scheme are given in [13,10].) In the first iteration $\psi^{(n+1)}$ is obtained by solving the following equation:

$$\nabla^2 \psi^{(n+1)}(x, y) = -\lambda^{(n)} \mathcal{F}\left(\psi^{(n)}, x, y\right) + \frac{1}{x}\frac{\partial \psi^{(n)}}{\partial x} \equiv g^{(n)},$$

in a manner similar to Eqs. (16)–(17). The eigen pair $(\lambda^{(n)}, \psi^{(n)})$ are normalized in each iteration using L^∞-norm of $\psi^{(n)}$:

$$\lambda^{(n+1)} = \frac{\lambda^{(n)}}{\left\|\psi^{(n)}\right\|_{L^\infty}}, \qquad \psi^{(n+1)} = \frac{\psi^{(n)}}{\left\|\psi^{(n)}\right\|_{L^\infty}}. \tag{19}$$

The iterations are continued till the L^∞-error, E′, defined by,

$$\mathrm{E}' = \frac{\left\|\psi^{(n+1)} - \psi^{(n)}\right\|_{L^\infty}}{\left\|\psi^{(n)}\right\|_{L^\infty}} \tag{20}$$

attains a certain minimum value. In this case usually the exact solution is not known, hence we use E′ given above to check the convergence [7].

4. Numerical results

As mentioned earlier three choices of right hand side of the GS equation are used in this work. The expressions of right hand side, and the corresponding numerical solutions using the method explained in the previous section are presented here.

4.1. Solov'ev solutions-I

In Solov'ev solution, the right hand side of GS equation is approximated by certain monomials of x or y, for example [23]:

$$-\triangle^* \psi = \frac{\gamma}{1+\alpha^2} - x^2. \tag{21}$$

The exact solution of the above equation is given as [23]:

$$\psi = \frac{1}{2\left(1+\alpha^2\right)}\left[\left(x^2-\gamma\right)y^2 + \frac{\alpha^2}{4}\left(x^2-1\right)^2\right]. \tag{22}$$

For the numerical results presented in this work, we take $\alpha = \sqrt{2}$ and $\gamma = 0.25$ as in [23]. To compare the numerical solution with the exact solution the boundary Γ is created using the exact solution implicitly. In Fig. 2(a) we plot the exact solution and extract the closed curve on which $\psi \equiv \bar{\psi} = 0.043$, which becomes the boundary condition (BC) for the numerical solution. The comparison of the numerical solution of Eq. (2) with the analytical solution as given in Eq. (22) is applicable within this boundary. In general the solution ψ is required in the whole domain because the boundary Γ is not known a priori. The numerical solution outside Γ is obtained by solving the homogeneous GS equation, i.e., $-\triangle^* \psi = 0$. The interface of the two regions becomes quite complex [23,9]. However a lot of theoretical understanding about tokamak plasma can be developed by considering the free boundary as a fixed boundary.

The analytical expressions for x and y components of the magnetic field and the toroidal current density corresponding to the above solution are as given below:

$$B_x = -\frac{1}{x}\frac{\partial \psi}{\partial y} = \frac{\left(\gamma - x^2\right)y}{\left(1+\alpha^2\right)x}, \tag{23}$$

$$B_y = \frac{1}{x}\frac{\partial \psi}{\partial x} = \frac{\left(x^2-1\right)\alpha^2 + 2y^2}{2\left(1+\alpha^2\right)}, \tag{24}$$

$$j_\phi = -\frac{1}{x}\triangle^* \psi = \frac{1}{x}\left(\frac{\gamma}{1+\alpha^2} - x^2\right). \tag{25}$$

The numerical values of B_x and B_y can be obtained using the expressions for the derivatives given in Eqs. (12) and (13) which require Eqs. (A.2) and (A.3). Similarly j_ϕ, in Eq. (25) can be calculated numerically using

$$\begin{aligned} j_\phi &= -\frac{1}{x}\triangle^* \psi \\ &= -\frac{1}{x}\left(\nabla^2 \psi - \frac{1}{x}\frac{\partial \psi}{\partial x}\right) \end{aligned}$$

which can be approximated using Eqs. (5), (6) and (12)

$$\begin{aligned} \left(j_\phi\right)_i &= -\sum_{j=1}^{n_d} a_j \left\{\left(\nabla^2 \hat{\psi}\right)_{ij} - \frac{1}{x_i}\left(\frac{\partial \hat{\psi}}{\partial x}\right)_{ij}\right\} \\ &= -\sum_{j=1}^{n_d} a_j \left\{f_{ij} - \frac{1}{x_i}\left(\frac{\partial \hat{\psi}}{\partial x}\right)_{ij}\right\}. \end{aligned} \tag{26}$$

The geometry, boundary points and domain points are shown in Fig. 2(a). The nodes are created using MATLAB function "polygon" and further refinement is accomplished by Centroidal Voronoi Tessellations (CVT) algorithm.[1] This algorithm creates n_d partitions of Ω such that each point of a given partition is closest to the centroid of that partition than the centroid of any other partition. The domain point in Ω are located at these centroids.

Following the procedure outlined in Section 3 and choosing the shape parameter σ in the MQ-RBF as the average of the geometrical dimension, $\sigma = \left(|x_{\max} - x_{\min}| + |y_{\max} - y_{\min}|\right)/2$, the numerical results are obtained. The convergence curve with respect to an exact solution for a typical value of $n_d = 256$, and $n_b = 256$ is shown in Fig. 2(b), where L^∞-error E (Eq. (18)) (which is the maximum error in the solution) decreases and saturates within 5–10 iterations. On increasing the number of domain points (n_d) and the boundary points (n_b) the solutions of ψ, B_x, B_y and j_ϕ improve as shown in Fig. 2(c), (d), (e), (f). We see that the convergence curves of B_x, B_y and j_ϕ saturate early compared to the curve of ψ. This is because they involve the derivatives of ψ, Eqs. (23)–(26). The numerical calculation of derivatives of ψ is less accurate than that of ψ itself because they involve the nonradial coordinates (x or y coordinates) as can be seen in Eqs. (A.2) and (A.3).

[1] people.sc.fsu.edu/~jburkardt/m_src/cvt/cvt.html.

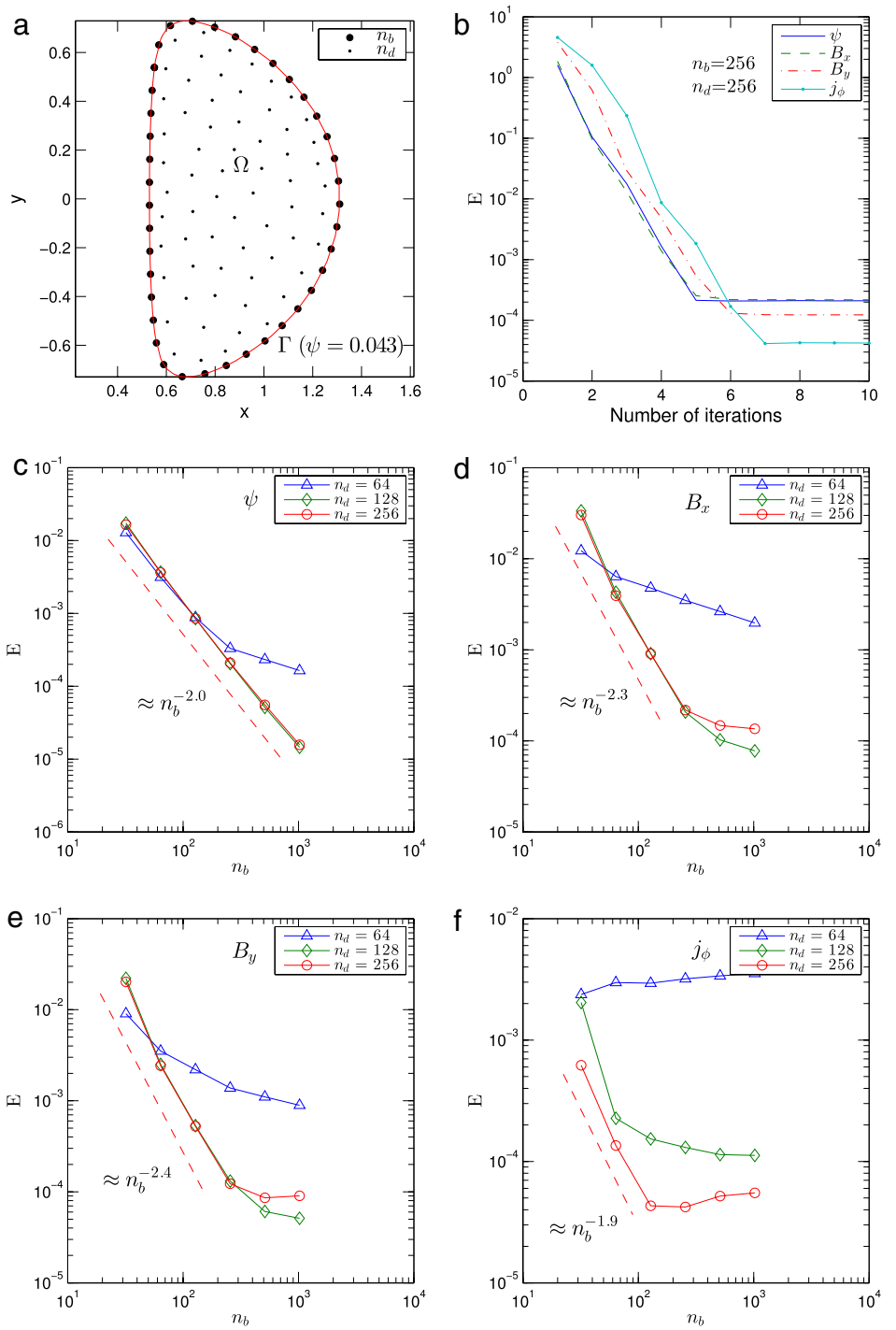

Fig. 2. Solov'ev solutions-I: (a) The geometry, boundary and internal nodes, (b) the convergence curves for ψ, B_x, B_y, and j_ϕ with respect to the number of iterations; (c–f): the convergence curves for ψ, B_x, B_y, and j_ϕ with respect to n_b and n_d.

In Fig. 2(c), (d), (e), (f) we also observe that increasing the number of boundary points has a more pronounced effect on the accuracy than increasing the number of domain points. However, the accuracy does not improve after certain values of n_b and n_d due to the effect of ill-conditioning (which is inherent in the global RBFs based meshless methods [15,19]). The reason behind it is the dense nature of matrix A resulting from the global RBFs. It can be seen in Fig. 2(c), (d), (e), (f) that the error in the computed solution decreases almost quadratically with respect to number of boundary points.

Fig. 3(a) shows the boundary Γ ($\psi = 0.043 = \bar{\psi}$). The exact solution is plotted inside as well as outside of Γ and numerical solution is compared only inside Γ. The relative accuracy of the solution inside Γ for $n_d = 256$, and $n_b = 256$ is

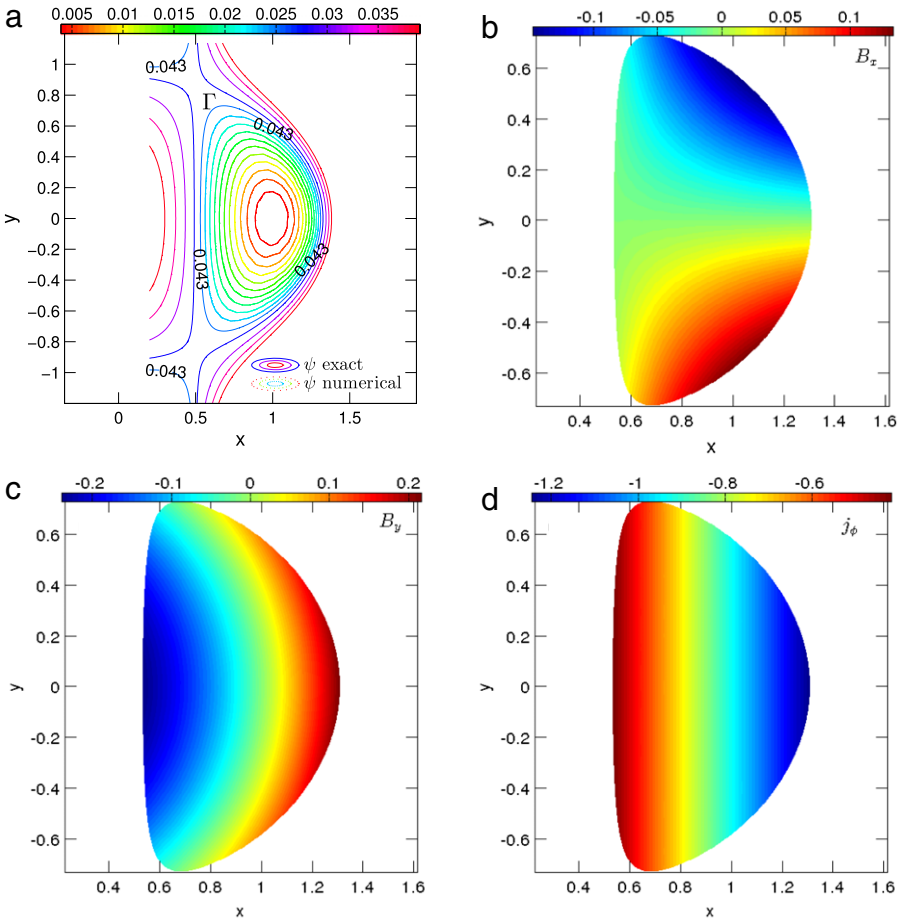

Fig. 3. Solov'ev solutions-I ($n_b = 256$ and $n_d = 256$): (a) Comparison of numerical and analytical solutions of ψ inside the boundary $\Gamma(\psi = 0.043 = \bar{\psi})$ (the contours outside Γ show the analytical solution only); (b–d): the numerical solutions of B_x, B_y, and j_ϕ.

E $\sim 10^{-4}$ (Fig. 2(b)). The numerical solution of B_x, B_y and j_ϕ corresponding to $n_d = 256$, and $n_b = 256$ can also be seen in Fig. 3(b), (c), (d) which also have the relative accuracy E $\sim 10^{-4}$ (Fig. 2(b)).

4.2. Solov'ev solutions-II

To see the applicability of the method for the geometry where a magnetic X-point is present, the following example is considered [6]:

$$\triangle^* \psi = (1 - A)\, x^2 + A. \tag{27}$$

The solution of the above equation is given by

$$\psi(x, y) = \frac{x^4}{4} + A\left(\frac{1}{2}x^2 \ln x - \frac{x^4}{8}\right) + c_1\psi_1 + c_2\psi_2 + c_3\psi_3 + c_4\psi_4 + c_5\psi_5 + c_6\psi_6 + c_7\psi_7 + c_8\psi_8 + c_9\psi_9 + c_{10}\psi_{10} + c_{11}\psi_{11} + c_{12}\psi_{12}, \tag{28}$$

in the computational domain Ω surrounded by the boundary drawn using the implicit equation $\psi(x, y) = 0$. We evaluate the coefficients c_1–c_{12} in Eq. (28) by the method described in [6] with the help of the software MAPLE [24]. These coefficients and the expression of ψ_1 to ψ_{12} [6] are listed in Appendix B. The other parameters used in the computation of coefficients are: the inverse aspect ratio $\epsilon = 0.32$; elongation $\kappa = 1.70$; triangularity $\delta = 0.330$; $x_{sep} = 0.88$; $y_{sep} = -0.60$ and $A = -0.155$, where $x_{sep} = 1 - 1.1\delta\epsilon$ and $y_{sep} = -1.1\kappa\epsilon$. The details can be found in [6].

The geometry, boundary points and domain points for the above problem are shown in Fig. 4(a). The convergence of the variables ψ, B_x, B_y and j_ϕ is shown in Fig. 4(b) where the error E $\sim 10^{-3}$–10^{-4} is obtained for $n_b = 256$ and $n_d = 256$ in $\sim$10 iterations. In this example, the error E in ψ scales as E $\propto n_b^{-1.7}$ (Fig. 4(c)) and E $\propto n_d^{-3.6}$ (Fig. 4(d)). The numerical

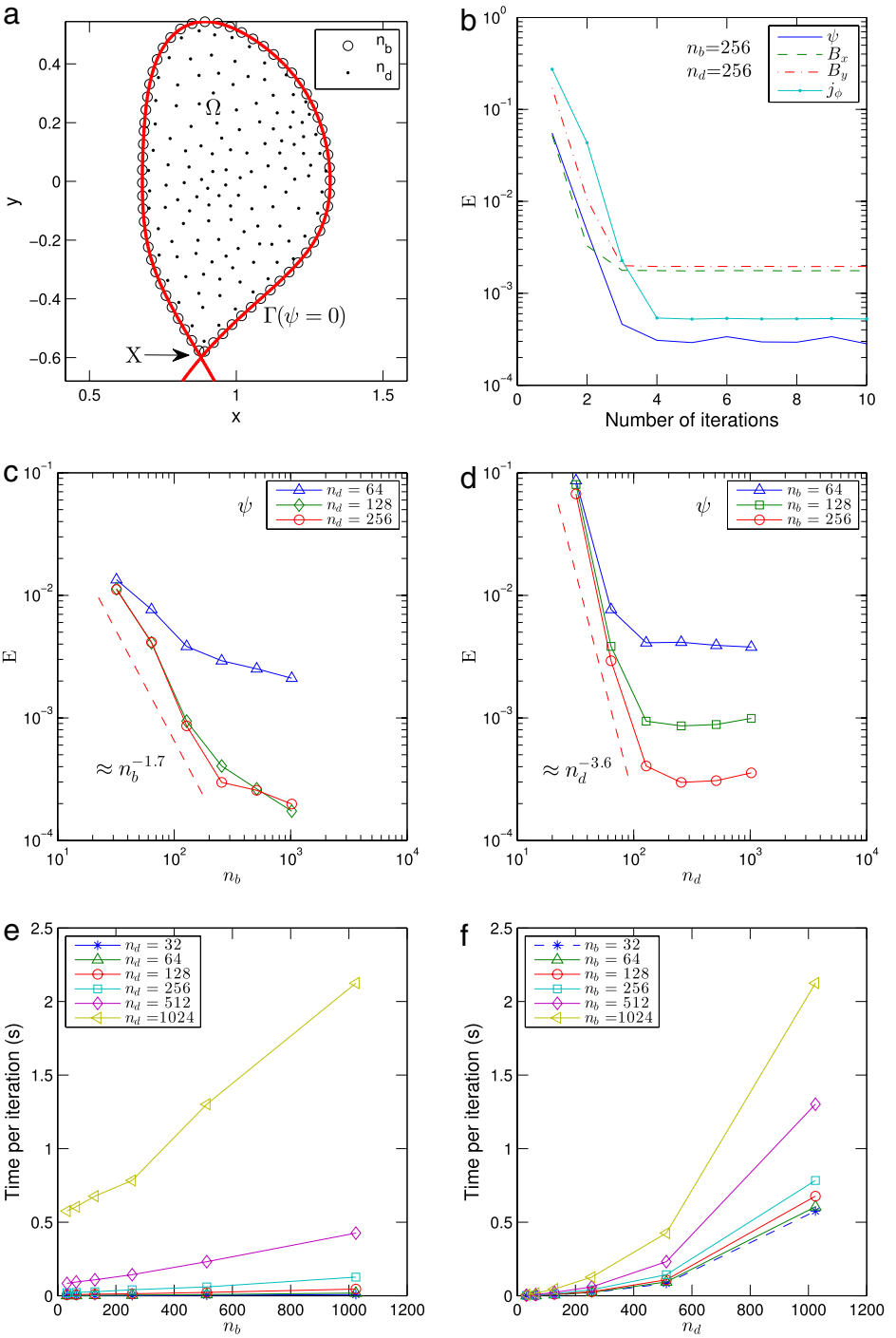

Fig. 4. Solov'ev solutions-II: (a) The geometry, boundary and internal nodes, (b) the convergence curves for ψ, B_x, B_y, and j_ϕ with respect to the number of iterations; (c) The convergence curves of ψ with respect to n_b for various n_d, (d) The convergence curves of ψ with respect to n_d for various n_b, (e) computation time vs. n_b, and (f) computation time vs. n_d (see text in Section 4.2 for machine specifications).

solution for ψ, B_x, B_y and j_ϕ corresponding to $n_d = 256$, and $n_b = 256$ can also be seen in Fig. 5(a), (b), (c), (d) which also have the relative accuracy E $\sim 10^{-3}$ to 10^{-4} (Fig. 4(b)).

The computation time taken by the method for different n_b and n_d is shown in Fig. 4(e), (f). The elapsed time is computed in MATLAB 2012a [21] installed in 64-bit UBUNTU-LINUX. The computer used for the simulations has 4 GB RAM, Intel-Core-i5-4670 CPU, and 3.40 GHz $\times$ 4 cores. It is seen that maximum time consumed for $n_b = 1024$ and $n_d = 1024$, i.e., $n_t\ (= n_b + n_d) = 2048$ is 2.1 s per iteration which means that the converged solution can be obtained in approximately 21 s.

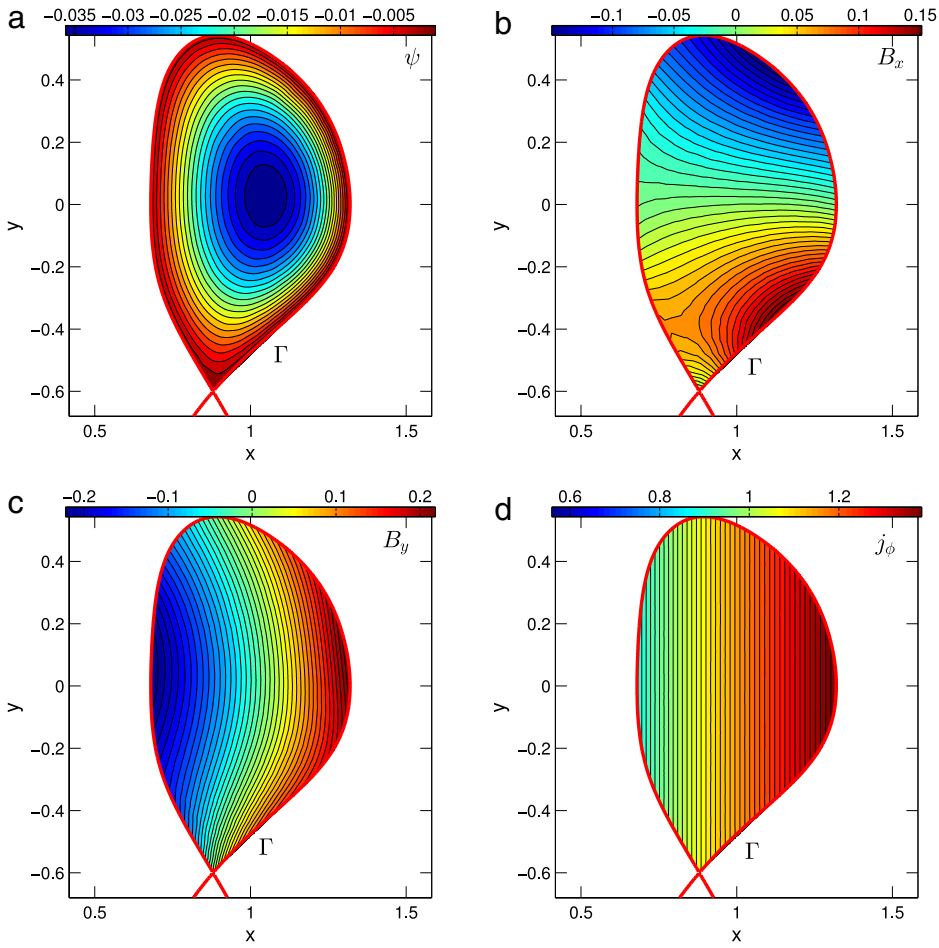

Fig. 5. Solov'ev solutions-II: (a–d): the numerical solution of ψ, B_x, B_y, and j_ϕ with respect to n_b and n_d for $n_b = 256$ and $n_d = 256$.

4.3. The GS equation with linear right hand side

In this case, the right hand side is chosen as a linear function of ψ. We consider the following example given in [25]: Here the following nondimensionalization is used $R \to ax, Z \to ay,\ \Psi \to \Psi_0\psi, B_R \to \left(\Psi_0/a^2\right) B_x, B_Z \to \left(\Psi_0/a^2\right) B_y$, and $J_\Phi \to \left(\Psi_0/\mu_0 a^3\right) j_\phi$, where a the minor radius (Fig. 1(a)) and Ψ_0 is an arbitrary value magnetic flux. For this case, the GS equation is:

$$-\triangle^*\psi = \left(x^2+1\right)\left(\psi + \frac{1}{2}\right). \tag{29}$$

The solution of the above equation is given by

$$\psi(x,y) = \cos\left(\frac{x^2}{2}\right)\cos(y) - \frac{1}{2}, \tag{30}$$

in the computational domain Ω surrounded by the boundary Γ ($\psi = 0 = \bar{\psi}$) defined by the following [25]:

$$x \in \left[\frac{2}{3}\sqrt{3\pi}, \frac{2}{3}\sqrt{6\pi}\right],$$

$$y \in \left\{\cos^{-1}\left(\frac{1}{2\cos\left(x^2/2\right)}\right)\right\} \cup \left\{2\pi - \cos^{-1}\left(\frac{1}{2\cos\left(x^2/2\right)}\right)\right\}.$$

The exact expression for x and y components of the magnetic field and the toroidal current density can be calculated using the formulae of B_x, B_y and j_ϕ in Eqs. (23)–(25), and are written below:

$$B_x = \frac{1}{x}\cos\left(\frac{x^2}{2}\right)\sin(y) \tag{31}$$

$$B_y = -\sin\left(\frac{x^2}{2}\right)\cos(y) \tag{32}$$

$$j_\phi = \frac{1}{x}\left(x^2+1\right)\cos\left(\frac{x^2}{2}\right)\cos(y)\,. \tag{33}$$

The geometry, boundary points and domain points for the above problem are shown in Fig. 6(a). It can be seen in Fig. 6(b) that the solution converges to sufficient relative accuracy E $\sim 10^{-3}$–10^{-4} (Eq. (18)) after 10–15 iterations for $n_d = 256$, and $n_b = 128$. Convergence of the numerical solution for different values of n_b and n_d in Fig. 6(c) again shows, as in the earlier case (Solov'ev solutions), that increasing n_b in comparison to n_d is more effective. The solution does not improve after certain number of points (n_b and n_d) due to dominance of ill-conditioning.

In this example, the error E in ψ scales as E $\propto n_b^{-2.1}$ (Fig. 6(c)) and E $\propto n_d^{-4.1}$ (Fig. 6(d)). For B_x, it scales as E $\propto n_b^{-2.0}$ (Fig. 6(e)) and E $\propto n_d^{-3.6}$ (Fig. 6(f)). In these figures we also see that for higher values of n_b or n_d the accuracy diminishes due to increased ill-conditioning of the coefficient matrix.

The contours for the converged numerical solution of ψ, B_x, B_y and j_ϕ are shown in Fig. 7(a), (b), (c), (d). In Fig. 7(a), the exact solution of ψ (contours with black solid lines) and numerical solution of ψ (contours with red dashed lines) are too close to be distinguished. The numerical solutions of B_x, B_y and j_ϕ are shown in Fig. 7(b), (c), (d) with their accuracies in Fig. 6(c).

4.4. Nonlinear eigen value problem

The GS-equation is usually solved as a nonlinear eigen value problem. The eigen value λ is introduced in the nonlinear right hand side as shown below [5]:

$$-\triangle^*\psi = \lambda\mathcal{F}(\psi, x, y) \tag{34}$$

where $xj_\phi = \lambda\mathcal{F}(\psi, x, y)$. A typical nonlinear parametric profile of $\mathcal{F}(\psi, x, y)$ can be considered in the following form [26,5]:

$$\mathcal{F}(\psi, x, y) = c_0\left\{\beta_p x^2 + \left(1-\beta_p\right)\right\}\mathcal{F}_1(\psi, x, y) \tag{35}$$

where $\mathcal{F}_1(\psi, x, y)$ can be taken as a polynomial in ψ or an exponential form, for example, $e^{-\gamma^2(1-\psi^2)}$ with γ as a parameter. We choose $\mathcal{F}_1(\psi, x, y) = \psi + \gamma_1\psi^2 + \gamma_2\psi^3$ with $\gamma_1 = 0.7$ and $\gamma_2 = 0.8$. The other parameters are chosen as $c_0 = 0.5$, $\beta_p = 0.6$ and the initial eigen pair as ($\lambda = 10$, $\psi = 1$). The solution is sought in the domain defined by the boundary Γ given by

$$x = 1 + \epsilon\cos(\theta + \alpha\sin\theta)$$
$$y = \epsilon\kappa\sin\theta$$

where the boundary condition $\psi = 0$ is imposed. Choosing the parameters, the inverse aspect ratio $\epsilon = 0.32$, elongation $\kappa = 1.70$ and $\alpha = \sin^{-1}(\delta)$, where triangularity $\delta = 0.33$, makes the boundary similar to the boundary of an ITER-*like* plasma [27] and is shown in Fig. 8(a).

The inverse iteration algorithm given in [7] is used here, as has been explained at the end of the Section 3. A typical convergence curve is shown in Fig. 8(b) where the error E′ (Eq. (20)) decreases with the number of iterations. The numerically calculated contours of ψ, B_x, B_y and j_ϕ are shown in Fig. 8(c), (d), (e), (f). It can be seen that the flux ψ and j_ϕ show the peak near the center.

5. Conclusion

The Grad–Shafranov (GS) equation has been solved for the fixed boundary tokamak equilibria using a meshless method based on approximate particular solutions. Unlike some other meshless methods, the method used in the present work does not require an exact particular solution nor the fundamental solution or any other homogeneous solutions, which tend to be very complex for the GS operator. In the scheme presented here, the GS equation is rearranged such that the left hand side of the equation consists of a two-dimensional Laplace operator. This allows us to use the radial basis functions (RBFs) and the corresponding particular solutions which are also radial. The GS equation is then solved for four characteristic cases involving linear and nonlinear dependence on the magnetic flux. In each case we solve the resulting over-determined system of algebraic equations using a least squares approach. The numerical results are presented using multiquadratic (MQ)-RBFs. The convergence behavior with respect to the number of boundary and domain points is presented. Comparison with the exact solution wherever available shows good agreement (relative error of the order of 10^{-4}) between the computed and analytical solutions. Further improvement may however be possible using localized meshless methods or compactly supported (CS)-RBFs [28,20,19] which help in reducing the ill-conditioning of the coefficient matrix.

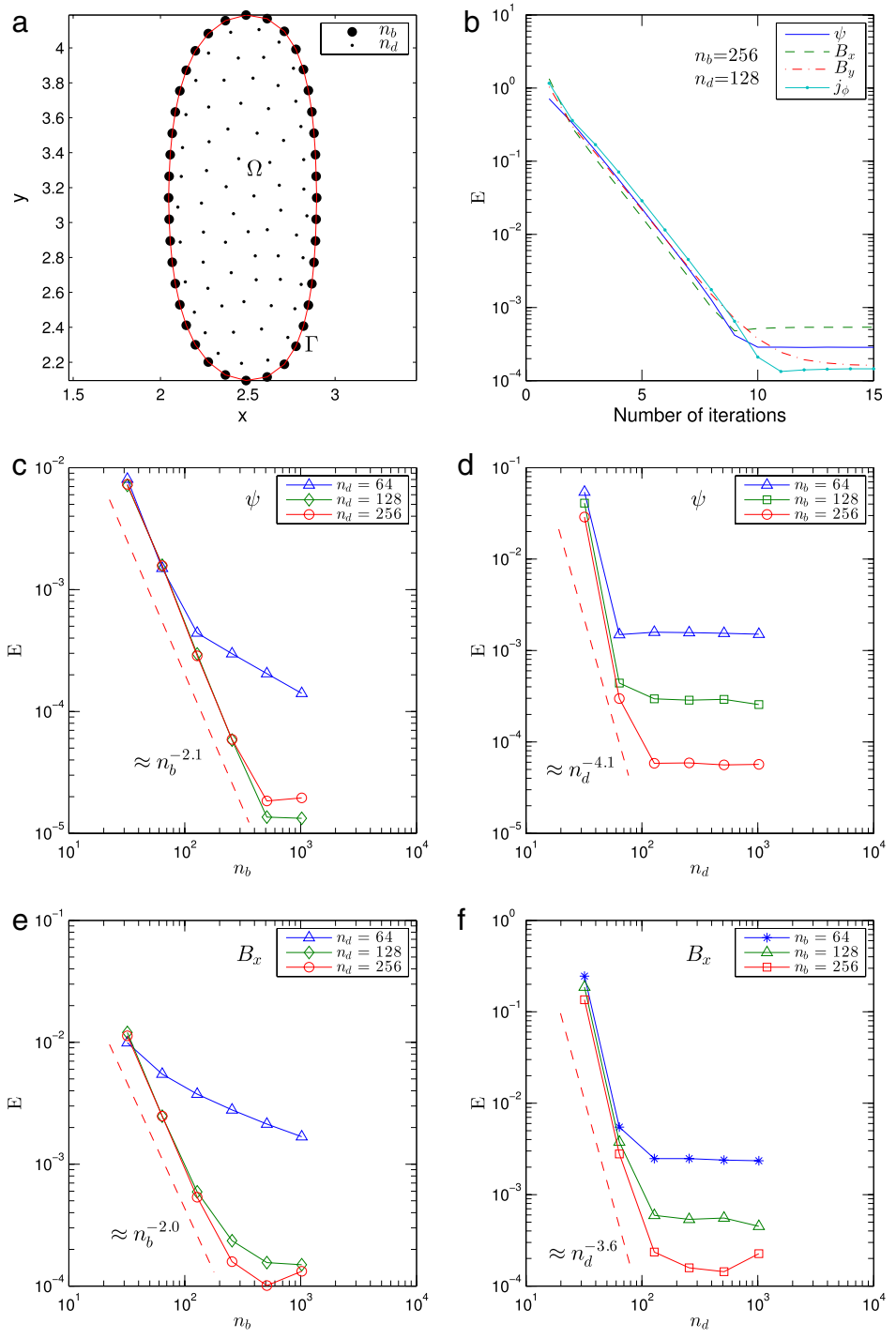

Fig. 6. Linear right hand side case: (a) The geometry, boundary and internal nodes, (b) the convergence curves of ψ, and B_x, B_y, and j_ϕ with respect to the number of iterations; (c–d): the convergence curves for ψ and B_x with respect to n_b and n_d. (For interpretation of the references to color in this figure legend, the reader is referred to the web version of this article.)

Appendix A

The particular solution corresponding to the MQ-RBF is given by [19],

$$\left(\hat{\psi}\right)_{ij} = \left(\frac{4\sigma^2 + r_{ij}^2}{9}\right)\sqrt{r_{ij}^2 + \sigma^2} - \frac{\sigma^3}{3}\ln\left(\sigma + \sqrt{r_{ij}^2 + \sigma^2}\right) \tag{A.1}$$

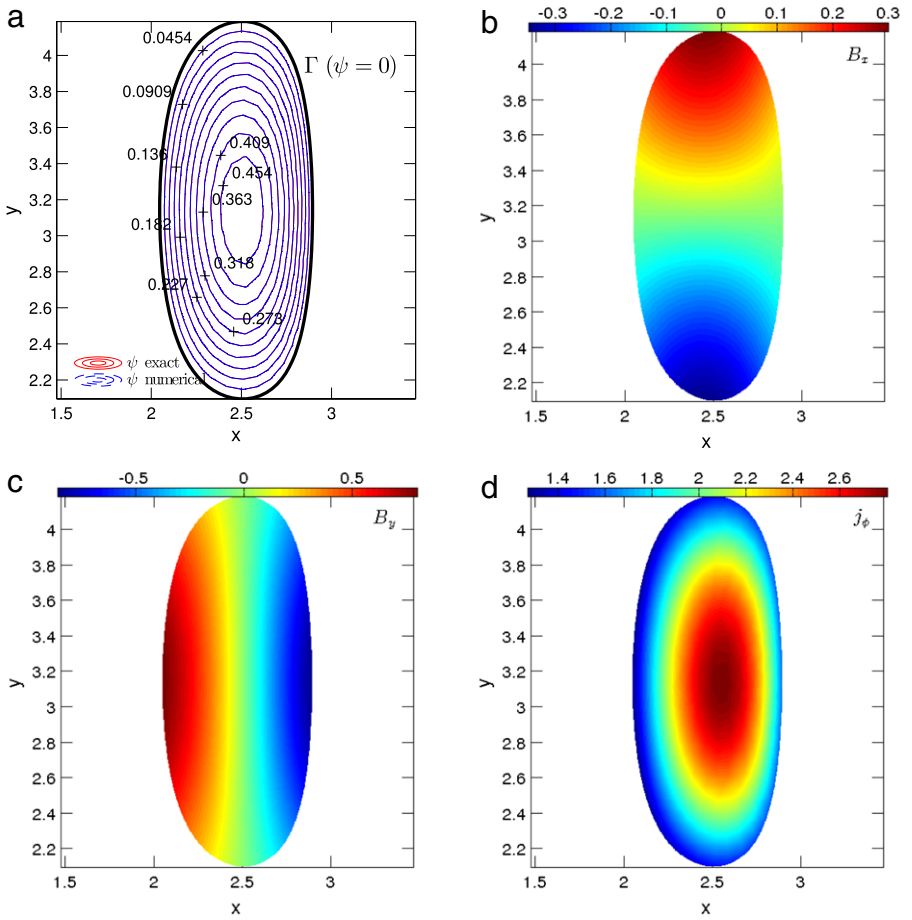

Fig. 7. Linear right hand side case ($n_b = 256$ and $n_d = 128$): (a) Comparison of numerical and analytical solutions of ψ; (b–d): the numerical solution of B_x, B_y, and j_ϕ. (For interpretation of the references to color in this figure legend, the reader is referred to the web version of this article.)

and its derivatives with respect to x and y:

$$\left(\frac{\partial \hat{\psi}}{\partial x}\right)_{ij} = \frac{x_i - x_j}{3}\left(\sigma + \frac{r_{ij}^2 + \sigma^2}{\sigma + \sqrt{r_{ij}^2 + \sigma^2}}\right) \tag{A.2}$$

$$\left(\frac{\partial \hat{\psi}}{\partial y}\right)_{ij} = \frac{y_i - y_j}{3}\left(\sigma + \frac{r_{ij}^2 + \sigma^2}{\sigma + \sqrt{r_{ij}^2 + \sigma^2}}\right). \tag{A.3}$$

Appendix B

The coefficients $c_1, c_2, \ldots, c_{12}$ are calculated using the method described in [6]:

$c_1 = 0.086491278547879$, $c_2 = 0.3236475999311122$, $c_3 = -0.5227047152014153$, $c_4 = -0.2319735789049058$, $c_5 = 0.3807375276921884$, $c_6 = -0.3573346678775671$, $c_7 = -0.0148740157319054$, $c_8 = 0.1480149379993053$, $c_9 = 0.7401867427139476$, $c_{10} = -0.4397718916520693$, $c_{11} = -0.1071308624644744$, $c_{12} = 0.0127862151469646$.

The expression of $\psi_1, \psi_2 \ldots \psi_{12}$ are given in [6]:

$$\psi_1 = 1$$
$$\psi_2 = x^2$$
$$\psi_3 = y^2 - x^2 \ln(x)$$
$$\psi_4 = x^4 - 4x^2y^2$$
$$\psi_5 = 2y^4 - 9x^2y^2 + 3x^4 \ln(x) - 12x^2y^2 \ln(x)$$

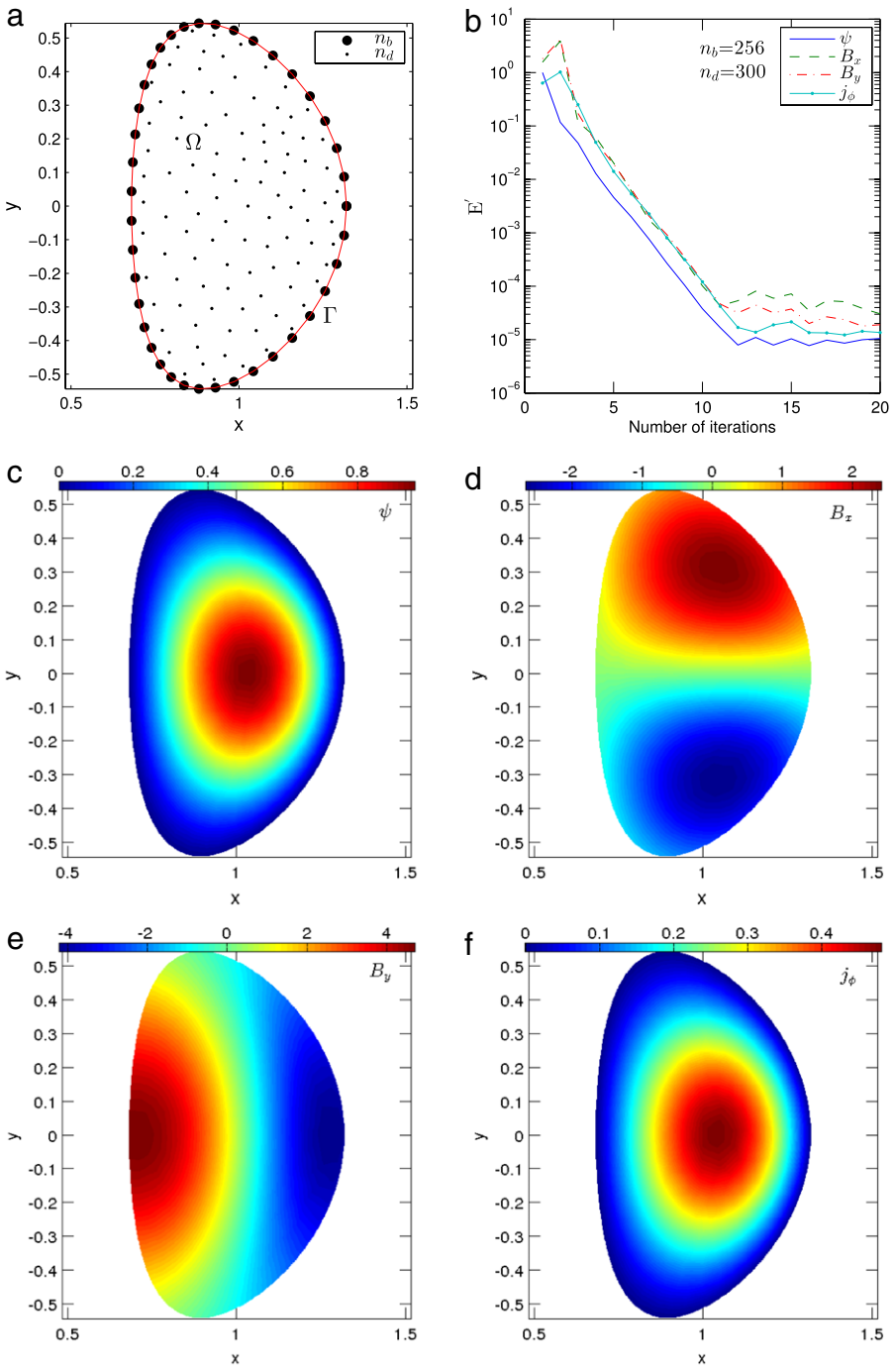

Fig. 8. Nonlinear right hand side case: (a) The geometry, boundary and internal nodes, (b) the convergence curves of ψ, B_x, B_y, and j_ϕ with respect to the number of iterations; (c–f): the numerical solution of ψ, B_x, B_y, and j_ϕ ($n_b = 256$ and $n_d = 300$).

$$\psi_6 = x^6 - 12x^4y^2 + 8x^2y^4$$
$$\psi_7 = 8y^6 - 140x^2y^4 + 75x^4y^2 - 15x^6 \ln(x) + 180x^4y^2 \ln(x) - 120x^2y^4 \ln(x)$$
$$\psi_8 = y$$
$$\psi_9 = yx^2$$
$$\psi_{10} = y^3 - 3yx^2 \ln(x)$$
$$\psi_{11} = 3yx^4 - 4y^3x^2$$
$$\psi_{12} = 8y^5 - 45yx^4 - 80y^3x^2 \ln(x) + 60yx^4 \ln(x)\,.$$

References

[1] H. Grad, H. Rubin, Hydromagnetic equilibria and force-free fields, in: Proceedings of the 2nd UN Conf. on the Peaceful Uses of Atomic Energy, Vol. 31, Geneva, 1958, p. 190.
[2] J.P. Freidberg, Ideal Magnetohydrodynamics, Plenum Press, New York, 1987.
[3] J. Blum, Numerical Simulation and Optimal Control in Plasma Physics: With Applications to Tokamaks, in: Modern Applied Mathematics Series, J. Wiley, 1989.
[4] T. Takeda, S. Tokuda, Computation of MHD equilibrium of tokamak plasma, J. Comput. Phys. 93 (1) (1991) 1–107.
[5] M. Itagaki, J. Kamisawada, S. Oikawa, Boundary–only integral equation approach based on polynomial expansion of plasma current profile to solve the Grad–Shafranov equation, Nucl. Fusion 44 (7) (2004) 811.
[6] A.J. Cerfon, J.P. Freidberg, "One size fits all" analytic solutions to the Grad–Shafranov equation, Phys. Plasmas 17 (3) (2010) 032502.
[7] A. Pataki, A.J. Cerfon, J.P. Freidberg, L. Greengard, M. O'Neil, A fast, high-order solver for the Grad–Shafranov equation, J. Comput. Phys. 243 (0) (2013) 28–45.
[8] J.P. Goedbloed, R. Keppens, S. Poedts, Advanced Magnetohydrodynamics With Applications to Laboratory and Astrophysical Plasmas, Cambridge University Press, 2010.
[9] S. Jardin, Computational Methods in Plasma Physics, in: Chapman & Hall/CRC Computational Science, CRC Press, 2010.
[10] A. Saitoh, T. Itoh, N. Matsui, A. Kamitani, H. Nakamura, Application of collocation meshless method to eigenvalue problem, Plasma Fusion Res. 7 (2406096) (2012).
[11] E. Giovannozzi, G. Calabrò, F. Crisanti, P. Micozzi, and EFDA ITM-TF contributors Use of radial basis functions for fixed boundary equilibrium reconstruction, in: 39th EPS Conference & 16th Int. Congress on Plasma Physics, Number P4.020, July 2012.
[12] D. Nath, M.S. Kalra, Solution of Grad–Shafranov equation by the method of fundamental solutions, J. Plasma Phys. 80 (2014) 477–494. 6.
[13] M. Itagaki, K. Nakada, H. Tanaka, A. Wakasa, Quasi-radial basis functions applied to boundary element solutions for the Grad–Shafranov equation, Eng. Anal. Bound. Elem. 33 (11) (2009) 1258–1272.
[14] G.E. Fasshauer, Meshfree Approximation Methods with MATLAB, in: Interdisciplinary Mathematical Sciences, vol. 6, World Scientific Publishing Company, 2007.
[15] C.S. Chen, A. Karageorghis, Y.S. Smyrlis (Eds.), The Method of Fundamental Solutions—A Meshless Method, Dynamic Publishers, Atlanta, 2008.
[16] D. Nath, M.S. Kalra, P. Munshi, One-stage method of fundamental and particular solutions (MFS-MPS) for the steady Navier–Stokes equations in a lid-driven cavity, Eng. Anal. Bound. Elem. 58 (0) (2015) 39–47.
[17] C.S. Chen, C.M. Fan, P.H. Wen, The method of approximate particular solutions for solving certain partial differential equations, Numer. Methods Partial Differential Equations 28 (2) (2012) 506–522.
[18] E.J. Kansa, Multiquadrics—a scattered data approximation scheme with applications to computational fluid-dynamics–II solutions to parabolic, hyperbolic and elliptic partial differential equations, Comput. Math. Appl. 19 (8–9) (1990) 147–161.
[19] W. Chen, Z.-J. Fu, C.S. Chen, Recent Advances on Radial Basis Function Collocation Methods, in: SpringerBriefs in Applied Sciences and Technology, Springer, Heidelberg, New York, Dordrecht, London, 2014.
[20] G. Yao, Local radial basis function methods for solving partial differential equations (Ph.D. thesis), University of Southern Mississippi, 2010.
[21] MATLAB. version 7.14 (R2012a). The MathWorks Inc., Natick, Massachusetts, 2012.
[22] L.S. Solov'ev, The theory of hydromagnetic stability of toroidal plasma configurations, Sov. J. Exp. Theor. Phys. 26 (1968) 400.
[23] D. Biskamp, Nonlinear Magnetohydrodynamics, in: Cambridge Monographs on Plasma Physics, vol. 1, Cambridge University Press, 1997.
[24] Maple. 13. Maplesoft, a division of Waterloo Maple Inc., Waterloo, Ontario.
[25] E. Deriaz, B. Despres, G. Faccanoni, K.P. Gostaf, L.M. Imbert-Gérard, G. Sadaka, R. Sart, Magnetic equations with FreeFem++ the Grad–Shafranov equation and the current hole, in: ESAIM Proc., Vol. 32, 2011, pp. 76–94.
[26] B.J. Braams, The interpretation of tokamak magnetic diagnostics, Plasma Phys. Control. Fusion 33 (7) (1991) 715–748.
[27] R. Aymar, P. Barabaschi, Y. Shimomura, The ITER design, Plasma Phys. Control. Fusion 44 (5) (2002) 519–565.
[28] G. Yao, J. Kolibal, C.S. Chen, A localized approach for the method of approximate particular solutions, Comput. Math. Appl. 61 (9) (2011) 2376–2387.